Hindawi
Advances in Materials Science and Engineering
Volume 2022, Article ID 4756272, 12 pages
https://doi.org/10.1155/2022/4756272

Research Article

Application of Honeycomb Structures in Key Components of Space Deployable Structures

Yang Yang[1,2], **Fan Wang**[1,2] **and Jieshan Liu**[1,2]

[1]*School of Mechanics and Construction Engineering, Jinan University, Guangzhou 510632, China*
[2]*Key Lab of Disaster Forecast and Control in Engineering, Ministry of Education, Guangzhou, Guangdong 510632, China*

Correspondence should be addressed to Fan Wang; twfan@jnu.edu.cn

Received 16 May 2022; Revised 2 October 2022; Accepted 17 October 2022; Published 8 November 2022

Academic Editor: Abílio De Jesus

The reed structure is the key component in the foldable space deployment mechanism. In the aerospace industry, weight loss occupies a pivotal position. The use of lightweight structure can achieve significant savings in launch costs and improve load efficiency. Aiming at the lightweight requirements of the space deployment mechanism, this paper discusses the substitution effect of the honeycomb topology on the reed structure in the space deployment structure. Firstly, the column structure of the honeycomb is equivalent to an orthotropic cylindrical block-shell structure. According to the bending theory of an orthotropic cylinder, the expanded honeycomb structure equivalent to an orthotropic cylindrical block-shell structure is deduced. Then, the exact expression of the reverse bending moment was obtained, and the bending moment-curvature curve during the folding process was drawn. The bending moment-curvature characteristics during the folding process are simulated by finite element numerical simulation. By proposing the index of unit mass for analysis and comparison, the results show that compared with the common spring steel structure, the honeycomb structure has better mechanical properties per unit mass and has a certain substitution effect on the reed structure.

1. Introduction

With the implementation of a series of major aerospace science and technology projects such as deep space exploration, manned spaceflight, and large-scale launch vehicles, space vehicles are prompted to use more space deployment mechanism accessories to meet their envelope space requirements. Limitations in the storage capacity of launch vehicles have prompted the increasing use of deployable structures for large space structures. Deployable structures such as solar sails and reflector antennas in large space structures can be packaged into a small volume prior to launch and deployed into a large configuration during space operation [1–5]. The reed-type space deployable structure is a new lightweight and efficient structure in the space deployment mechanism. Due to its excellent stiffness and strength, as well as the characteristics of ultra-light strength and ultra-light weight, it is very important to improve the space operation stability of spacecraft. It is of great significance to improve its spatial adaptability and operation ability. The reed structure is similar to the steel tape measure used in daily life, and the elastic strain energy accumulated during folding can be used to realize the automatic unfolding of the structure without other power devices. After deployment, it can rely on its own rigidity to provide the locking force required by the large-scale deployable structure without the need for additional locking devices. Traditional metal reeds are generally formed by beryllium-copper alloy or austenitic stainless-steel strips and cooperate with special heat treatment process to meet the final use requirements. They have been widely used in various deployment mechanisms of spacecraft [6–8].

Many solar panels for spacecrafts are deployed by tape spring hinges (TSHs) which have changeable stiffness. The stiffness of TSH is small when panels are folded, and it becomes large quickly in its deployed status. Figures 1–3 show its application in the solar panels. Sergio Pellegrino was the first to study the unfolding properties of reed structures

in combination with experiments [11]. Walker and Aglietti analyzed the bending properties of metal ribbon springs and studied the bending moment changes of the ribbon springs when they are buckling and torsionally deformed along their lengths [12]. Soykasap studied the performance of four different spring hinges. The behavior of the ribbon spring subjected to two-dimensional and three-dimensional folding was studied by the nonlinear finite element method, and the variation of the bending moment of the ribbon spring hinge with the rotation angle during the bending process was obtained [13, 14]. Xuan Jican and Wang conducted a theoretical study on the pure bending yield control of the ribbon spring and obtained the empirical formula that the material yielding does not occur during the bending process for the reduction of the unfolding performance caused by the possible material yielding of a single spring during the folding process [15]. The geometrically nonlinear behavior of ribbon springs was investigated experimentally and numerically by Dewalque et al. showing the characteristics of buckling, fold formation, and hysteresis [16–18]. Zuo et al. designed a carbon fiber ribbon spring through a theoretical analysis example and studied its buckling characteristics by combining finite element simulation and experiments [19].

Light weighting is a goal pursued by all designers. By reducing the weight, energy efficiency increases due to the decreasing energy consumption [20]. The aerospace industry is constantly looking to integrate advanced materials and manufacturing methods into their airframes to achieve new breakthroughs in lightweight design [21]. The principle of light weighting is to use less material or a material of lower density but ensure the same or enhanced technical performance. This paper explores the substitution effect of honeycomb topology on the reed structure in the folding and unfolding mechanism and studies the substitution effect of the traditional regular hexagonal honeycomb structure and the concave negative Poisson's ratio honeycomb structure in the reed structure. The mechanical properties of the sheet structures were compared. Through theoretical analysis, the honeycomb topology is equivalent to an orthotropic thin shell, and the calculation formula of the bending moment of the band spring of the honeycomb topology is deduced by using the orthotropic shell bending theory formula. The feasibility of negative Poisson's ratio honeycomb topology replacement is analyzed by theoretical and finite element simulations.

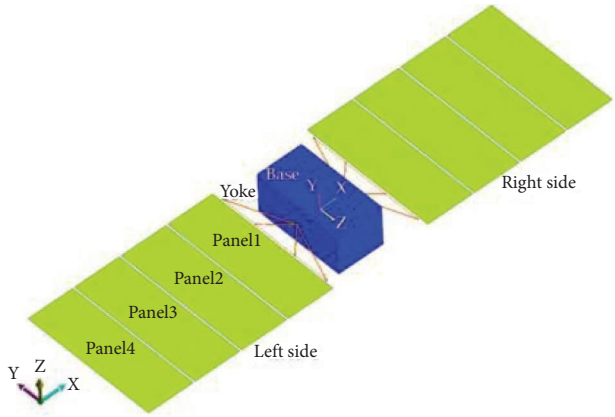

Figure 1: Model of a satellite system [9].

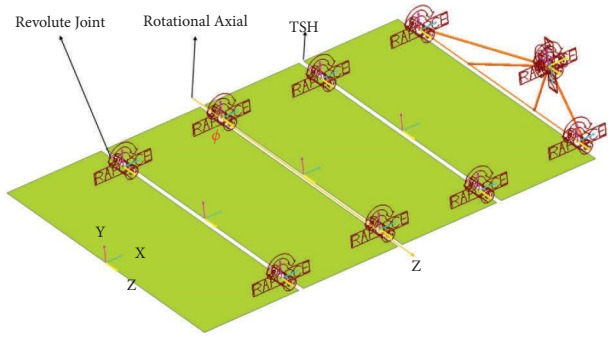

Figure 2: Modeling of tape spring hinges in RecurDyn.

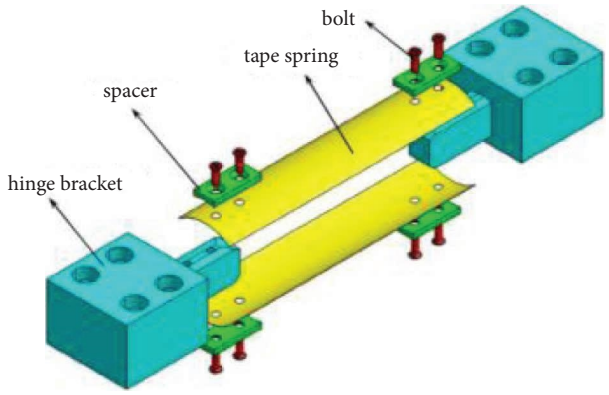

Figure 3: Tape spring hinge configuration [10].

2. Theoretical Analysis of Mechanical Properties of Ribbon Springs with Honeycomb Topology

2.1. Equivalent Parameters of Cellular Topology. When its strength is accessed, honeycomb material has conventionally been assumed to be a homogeneous plate due to its periodic cellular structure and can be efficiently analyzed by its equivalent elastic moduli. To date, extensive research into honeycombs consisting of regular hexagonal cells or symmetrical hexagonal cells has been carried out [22–25].

The earliest in-plane equivalent model for honeycomb cores was an "anti-plane" assumption proposed by Allen [26], which neglected the in-plane and bending stiffness of the core layer and considered only its lateral shear capacity. Allen's model greatly simplified the analysis and was therefore widely used in engineering in the early days. However, although the honeycomb core layer is soft, it has a large thickness compared to the skin, so its in-plane and bending stiffness should not be completely ignored. Gibson [24] and Burton and Noor [27] used the Bernoulli–Euler beam theory for honeycomb wall panels and gave equivalent

elastic parameter formulations for equal-wall-thickness honeycomb and double-wall-thickness honeycomb, respectively, under small deformation conditions.

In recent years, the research on the modeling methods of honeycomb sandwich structure has been continuously deepening. Tanimoto and co-workers proposed a new modeling method for honeycomb sandwich structure, in which orthogonal anisotropic shell elements and two kinds of beam elements were used to represent the panel, bonding layer, and honeycomb core, respectively [28]. It was pointed out that the vibration characteristics of honeycomb sandwich structure are closely related to the stiffness of the panel and the geometrical shape of the honeycomb core. Guj and Sestieri established an orthogonal anisotropic equivalent model of honeycomb using the multi-scale asymptotic technique, and the model was verified by the method of finite element numerical simulation [29].

In this paper, the application of the two honeycomb structures shown in Figure 1 in the ribbon spring is analyzed, and it is equivalent to an orthotropic structure with reference to Gibson. In the linear elastic range, the thin-walled honeycomb structure can be assumed to be an Euler–Bernoulli beam, and the tensile and compressive deformation of the thin-walled honeycomb can be regarded as nonnegligible compression deformation. The cell sizes of the two honeycomb structures are shown in Figure 4. For A-type honeycomb, t is the thickness of the inner wall of the honeycomb, l is the length of the vertical inner wall, $h$is the length of the inclined inner wall, and θ is the angle between the inclined inner wall and the horizontal direction. For B-type honeycomb, t is the thickness of the inner wall of the honeycomb, l is the length of the vertical inner wall, h is the length of the inclined inner wall, and θ is the angle between the inclined inner wall and the vertical direction.

Equivalent parameters of regular hexagonal honeycomb [30]:

$$\left.\begin{aligned} E_1 &= E_s\frac{t^3}{l^3}\frac{\cos\theta}{(\beta+\sin\theta)\sin^2\theta}\left(1-\cot^2\theta\frac{t^2}{l^2}\right)\\ \nu_{12} &= \frac{\cos^2\theta}{(\beta+\sin\theta)\sin\theta}\left(1-\csc^2\theta\frac{t^2}{l^2}\right)\\ E_2 &= E_s\frac{t^3}{l^3}\frac{(\beta+\sin\theta)}{\cos^3\theta}\left[1-\left(2\beta\sec^2\theta+\tan^2\theta\right)\frac{t^2}{l^2}\right]\\ \nu_{21} &= \frac{(\beta+\sin\theta)\sin\theta}{\cos^2\theta}\left[1-(2\beta+1)\sec^2\theta\frac{t^2}{l^2}\right]\\ G_{12} &= E_s\frac{t^3}{l^3}\frac{(\beta+\sin\theta)}{\beta^2(1+2\beta)\cos\theta} \end{aligned}\right\}. \quad (1)$$

Among them, $\beta = h/l$, and other parameters are shown in Figure 4(a).

For Model b, compared with Model a, its Poisson's ratio is negative, and the structure can also produce large deformation in a specific direction and has sufficient strength and stiffness in the direction that does not require deformation. Compared with the positive Poisson's ratio honeycomb core structure, the structure produces tensile deformation in one direction. The tensile deformation produced in the other direction is also a negative Poisson's ratio, and its in-plane equivalent parameter formula is [31]

$$\left.\begin{aligned} E_1 &= \left(\frac{t}{h}\right)^3\frac{E_s(h/l-\cos\theta)}{\sin^3\theta\left[1+\left(\cot^2\theta+l/t\csc^2\theta t/h\right)t^2/\mathrm{h}^2\right]}\\ \nu_{12} &= -\frac{\cos\theta(l/h-\cos\theta)\left(1-t^2/\mathrm{h}^2\right)}{h\sin^2\theta\left[1+\left(\cot^2\theta+l/t\csc^2\theta t/h\right)t^2/\mathrm{h}^2\right]}\\ E_2 &= \left(\frac{t}{h}\right)^3\frac{E_s}{\sin\theta(l/h-\cos\theta)\left(\cot^2\theta+t^2/\mathrm{h}^2\right)}\\ \nu_{21} &= -\frac{h\cos\left(1-t^2/\mathrm{h}^2\right)}{(l/h-\cos\theta)\left(\cot^2\theta+t^2/\mathrm{h}^2\right)}\\ G_{12} &= \frac{\mathrm{E_s t}^3}{\mathrm{hl}(l+2h)\sin\theta} \end{aligned}\right\}. \quad (2)$$

2.2. Theoretical Analysis of Folding Moment. For the unfolding mechanism, the main attention is on the value of the bending moment that produces folding. To obtain an accurate expression of the bending moment that produces folding and compare the unfolding bending moment of the isotropic ribbon spring and the weight-reduced negative Poisson's ratio honeycomb structure, the folding bending moments of the isotropic ribbon spring and the negative Poisson's ratio honeycomb structure are, respectively, derived below.

The geometric parameters of the ribbon spring are shown in Figure 5(a). The length of the ribbon spring is L, the radius of the circular section is R, the central angle is φ, the thickness of the circular section is t_0, and the arc length of the circular section is s. The bending and folding form is shown in Figure 5(b). The bending and folding rotation angle is φ, and the curvature radius is r.

The deformation after bending and folding is shown in Figure 6(a), and microelements are taken for analysis. The coordinate system shown in Figure 7 is established.

The cylindrical coordinate system shown in Figure 3 is used. Suppose the membrane force per unit width of the shell is $N(N_x, N_y, N_{xy})$, the bending internal force per unit width is

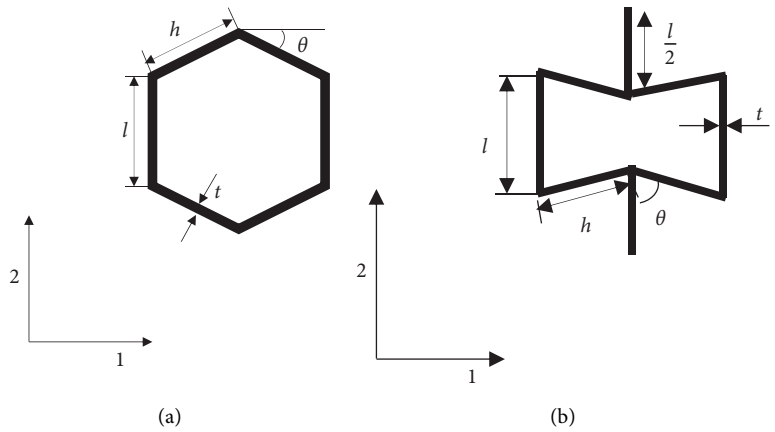

Figure 4: Structures of honeycomb. (a) Hexagon honeycomb. (b) Auxetic re-entrant honeycomb.

$M(M_x, M_y, M_{xy})$, the strain of the mid-plane is ε^0, and the deflection of the mid-plane is $\kappa(\kappa_x, \kappa_y, \kappa_{xy})$.

Constitutive equation:

$$\begin{bmatrix} N_x \\ N_y \\ N_{xy} \\ M_x \\ M_y \\ M_{xy} \end{bmatrix} = \begin{bmatrix} A_{11} & A_{12} & A_{16} & B_{11} & B_{12} & B_{16} \\ A_{12} & A_{22} & A_{26} & B_{12} & B_{22} & B_{26} \\ A_{16} & A_{26} & A_{66} & B_{16} & B_{26} & B_{66} \\ B_{11} & B_{12} & B_{16} & D_{11} & D_{12} & D_{16} \\ B_{12} & B_{22} & B_{26} & D_{12} & D_{22} & D_{26} \\ B_{16} & B_{26} & B_{66} & D_{16} & D_{26} & D_{66} \end{bmatrix} \begin{bmatrix} \varepsilon_x{}^0 \\ \varepsilon_y{}^0 \\ \gamma_{xy}{}^0 \\ \kappa_x \\ \kappa_y \\ \kappa_{xy} \end{bmatrix}. \tag{3}$$

For a special single-layer orthotropic laminate, the following results are obtained:

$$\left.\begin{aligned} A_{11} = Q_{11}t, D_{11} = \frac{Q_{11}}{12}t^3 \\ A_{12} = Q_{12}t, D_{12} = \frac{Q_{12}}{12}t^3 \\ A_{22} = Q_{22}t, B_{ij} \equiv 0, D_{22} = \frac{Q_{22}}{12}t^3 \\ A_{16} = A_{26} = 0, D_{16} = D_{26} = 0 \\ A_{66} = Q_{66}t, D_{66} = \frac{Q_{66}}{12}t^3 \end{aligned}\right\}, \tag{4}$$

$$Q = \begin{bmatrix} Q_{11} & Q_{12} & 0 \\ Q_{12} & Q_{22} & 0 \\ 0 & 0 & Q_{66} \end{bmatrix} = \begin{bmatrix} \dfrac{E_1}{1-\nu_{12}\nu_{21}} & \dfrac{\nu_{21}E_2}{1-\nu_{12}\nu_{21}} & 0 \\ \dfrac{\nu_{12}E_1}{1-\nu_{12}\nu_{21}} & \dfrac{E_2}{1-\nu_{12}\nu_{21}} & 0 \\ 0 & 0 & G_{12} \end{bmatrix}.$$

Then, the relationship between the bending moment per unit length and the curvature κ_x, κ_y (where $\kappa_{xy} = 0$) of the equivalent orthotropic shell honeycomb topology during the reverse bending process is

$$\begin{Bmatrix} M_x \\ M_y \end{Bmatrix} = \begin{bmatrix} D_{11} & D_{12} \\ D_{12} & D_{22} \end{bmatrix} \begin{Bmatrix} \kappa_x \\ \kappa_y \end{Bmatrix}. \tag{5}$$

Among them, κ_x, κ_y are the curvature changes of the honeycomb topology along the x and y directions during the bending process. Assuming that the shell changes from 0 to $1/r$ along the x direction after bending, then

$$\kappa_x = \frac{1}{r}, \kappa_y = \frac{1}{R} - \frac{\mathrm{d}^2 w}{\mathrm{d}y^2}. \tag{6}$$

Among them, w is the deflection of the honeycomb topology along the z direction; substituting (6) into (5), then

$$M_x = D_{11}\frac{1}{r} + D_{12}\left(\frac{1}{R} - \frac{\mathrm{d}^2 w}{\mathrm{d}y^2}\right), \tag{7}$$

$$M_y = D_{12}\frac{1}{r} + D_{22}\left(\frac{1}{R} - \frac{\mathrm{d}^2 w}{\mathrm{d}y^2}\right). \tag{8}$$

The following equilibrium differential equation is obtained by the energy method:

$$\left.\begin{aligned} r\frac{\mathrm{d}Q_y}{\mathrm{d}y} + N_x = 0, \\ \frac{\mathrm{d}M_y}{\mathrm{d}y} - Q_y = 0. \end{aligned}\right\}. \tag{9}$$

Eliminate Q_y; then,

$$\frac{\mathrm{d}^2 M_y}{dy^2} + \frac{N_x}{r} = 0. \tag{10}$$

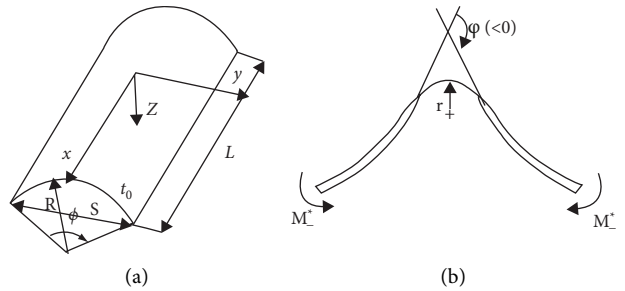

Figure 5: Geometrical parameters of tape springs and its folding types. (a). (b).

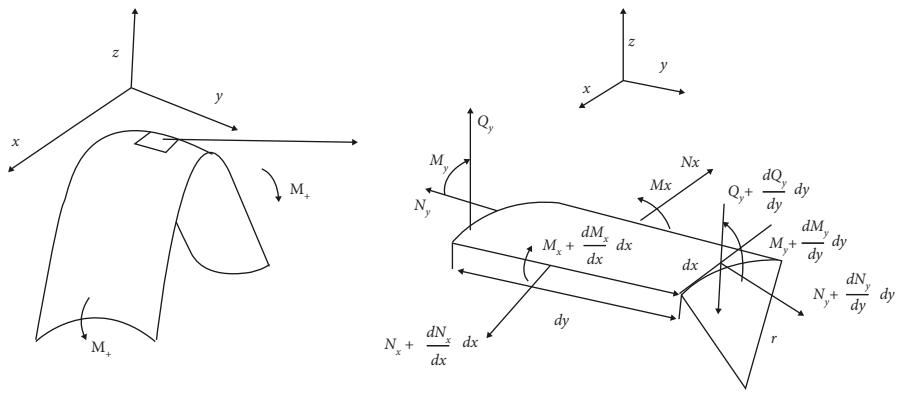

Figure 6: Microunit stress. (a). (b).

N_x is the normal force per unit length of the honeycomb topology:

$$N_x = A_{11}\varepsilon_x + A_{12}\varepsilon_y. \tag{11}$$

Among them,

$$z = 0, \varepsilon_x = \frac{w}{r}, \varepsilon_y = \frac{dv}{dy}. \tag{12}$$

Because $\varepsilon_y = \partial v/\partial y$, v is constant after bending, so $\varepsilon_y = 0$

.

$$N_x = -\frac{A_{11}w}{r}. \tag{13}$$

Substitute (13) into (10) to get

$$\frac{d^2M_y}{dy^2} - \frac{A_{11}w}{r^2} = 0. \tag{14}$$

Substitute (8) into (14) to get

$$\frac{d^4w}{\partial y^4} + \frac{A_{11}w}{D_{22}r^4} = 0. \tag{15}$$

Let $n = \sqrt[4]{A_{11}r^2/4D_{22}}$; then,

$$\frac{d^4w}{\partial y^4} + 4n^4\frac{w}{r^4} = 0. \tag{16}$$

The solution is

$$\begin{aligned} w = {} & e^{-(ny/r)}\left(c_1\cos\frac{ny}{r} + c2\sin\frac{ny}{r}\right) \\ & + e^{ny/r}\left(c_3\cos\frac{ny}{r} + c_4\sin\frac{ny}{r}\right). \end{aligned} \tag{17}$$

$w(y)$symmetry about y-axis: $c_1 = c_3, c_2 = -c_4$.

$$w = c_1\cosh\frac{ny}{r}\cos\frac{ny}{r} + c_2\sinh\frac{ny}{r}\sin\frac{ny}{r}. \tag{18}$$

Among them, $y = \pm s/2, s = 2R\sin(\theta/2)$ is the width of the cellular topology.

On the border, $y = \pm s/2$.

$$\frac{dM_y}{dy} = 0, M_y = 0. \tag{19}$$

Then,

$$\left.\begin{aligned} c_1 &= \frac{r^2}{2n^2}\left(\frac{1}{R} + \mu\kappa_x\right)\frac{\cosh ns/2r\sin ns/2r + \sinh ns/2r\cos ns/2r}{\cosh ns/2r\sinh ns/2r + \cos ns/2r\sin ns/2r} \\ c_2 &= -\frac{r^2}{2n^2}\left(\frac{1}{R} + \mu\kappa_x\right)\frac{\cosh ns/2r\sin ns/2r - \sinh ns/2r\cos ns/2r}{\cosh ns/2r\sinh ns/2r + \cos ns/2r\sin ns/2r} \end{aligned}\right\}. \tag{20}$$

Among them, $\mu = D_{11}/D_{22}$.

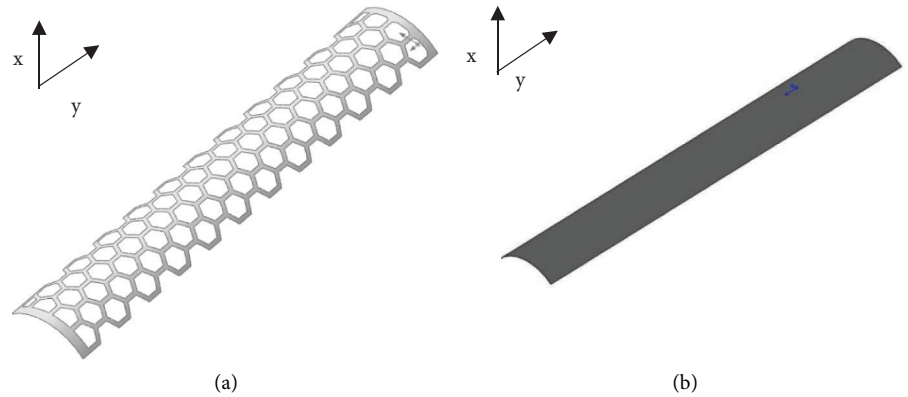

Figure 7: Tape spring with honeycomb structure. (a) Honeycomb structure. (b) Orthotropic structure.

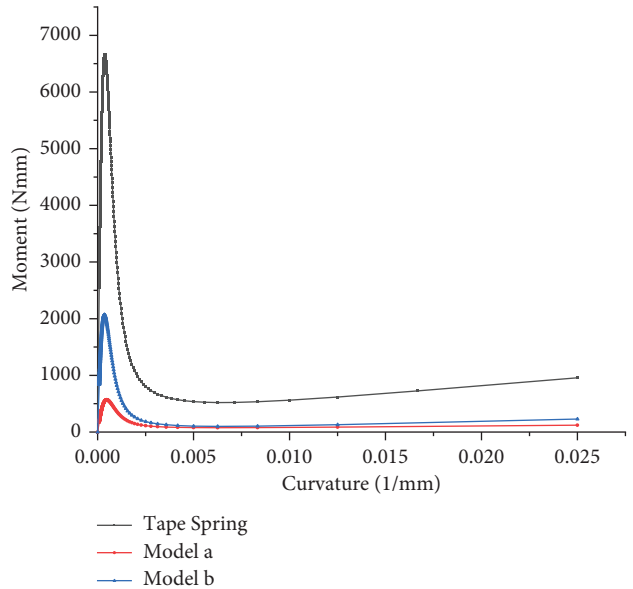

Figure 8: Bending moment-curvature curves of the three structures during the folding process.

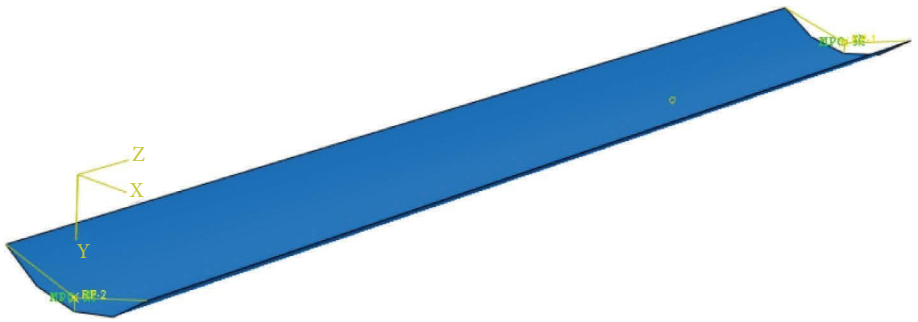

Figure 9: Finite element model of a single common spring steel band spring.

Table 1: Model geometry.

Parameters	Data
Length L/mm	350
Radius of central corner R/mm	35
Central angle of cross section α (rad)	1.57
Depth t/mm	0.2

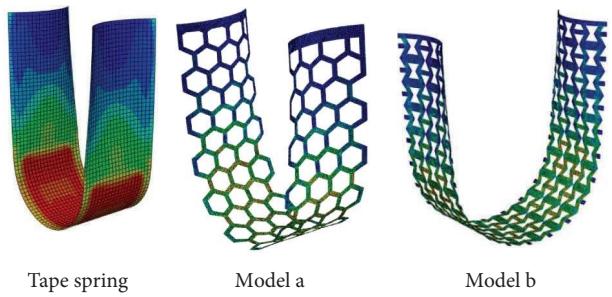

Figure 10: FEM for different structures.

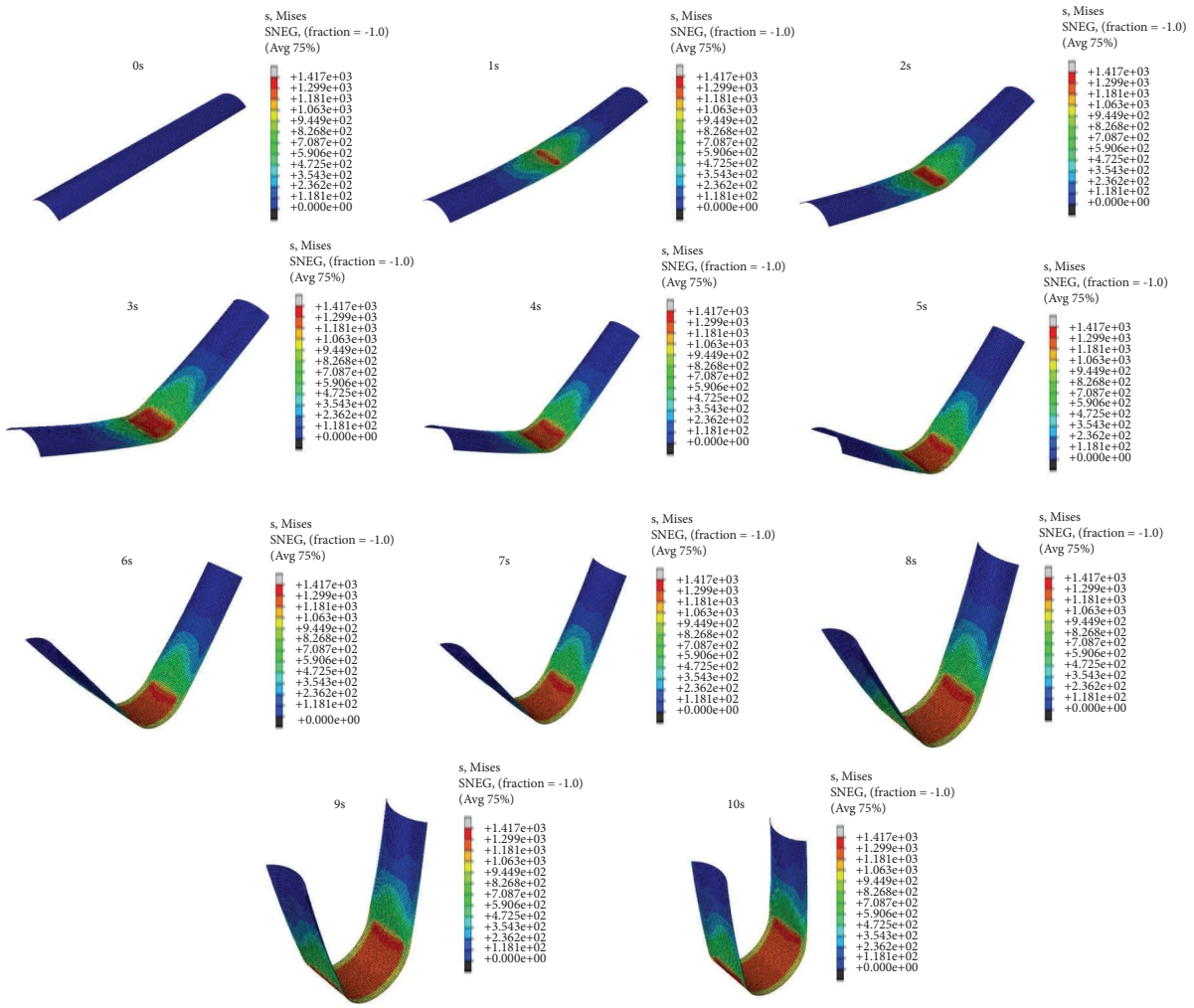

Figure 11: The fold deformation process of the tape spring.

Assuming that the bending moment required for driving in the bending process of the honeycomb topology is M, then M can be calculated by integrating:

$$M = \int_{-s/2}^{s/2} (M_x - N_x\omega)\mathrm{d}y = \frac{sE_1{t_0}^3}{12(1-\mu_{12}\mu_{21})}\left[\frac{1}{r} + \frac{\beta}{R} - \beta\left(\frac{1}{R} + \frac{\beta}{r}\right)F_1 + \left(1 + \frac{\beta R}{r}\right)^2 \frac{r}{R^2}F_2\right]. \tag{21}$$

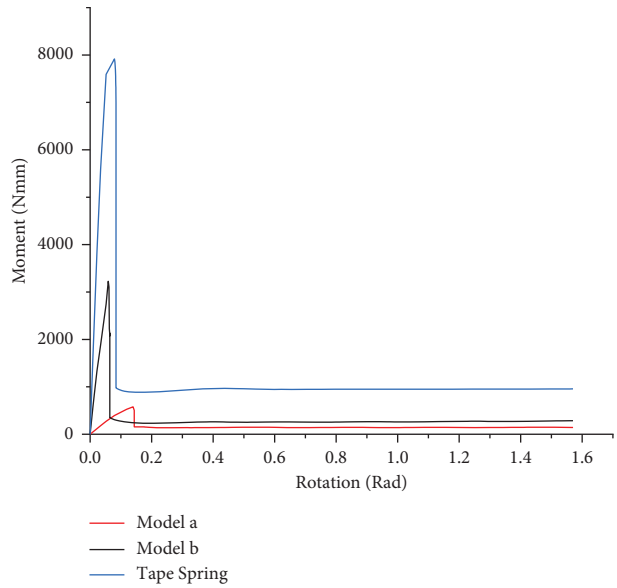

Figure 12: The moment-rotation angle relationships for different structures.

Among them, M_x and N_x represent the bending moment and membrane force per unit length in the x direction, w is the out-of-plane deflection, y is the longitudinal length of the honeycomb topology, and F_1, F_2 are

$$\left.\begin{aligned} F_1 &= \frac{2}{\lambda}\frac{\cosh\lambda - \cos\lambda}{\lambda\sinh\lambda + \sin\lambda}, \\ F_2 &= \frac{1}{2\lambda}\frac{\cosh\lambda - \cos\lambda}{\lambda\sinh\lambda + \sin\lambda} - \frac{\sinh\lambda\sin\lambda}{(\sinh\lambda + \sin\lambda)^2}. \end{aligned}\right\} \quad (22)$$

Among them, $\lambda = ns/r$. $M_+^{\max}$ is the maximum value of (21), and it is reflected as the critical bending moment of the honeycomb topology. The larger the value, the stronger the anti-interference ability of the honeycomb topology. It can be seen from the expression that M is related to material parameters and geometric parameters.

In order to explore the substitution effect of the honeycomb topology on the reed structure in the folding and unfolding mechanism, this paper established a common ribbon spring model with $L = 350$ mm, $R = 35$ mm, $\psi = \pi/2$, and $t_0 = 2$ mm. The geometric parameters of A-type honeycomb model are $L = 350$ mm, $R = 35$ mm, $\psi = \pi/2$, $\theta = \pi/6$, $t = 2$ mm, $t_0 = 2$ mm, $l = 10$ mm, $h = 10$ mm. The geometric parameters of B-type honeycomb are $L = 350$ mm, $R = 35$ mm, $\psi = \pi/2$, $\theta = \pi/6$, $t = 2$ mm,$t_0 = 2$ mm, $l = 10$ mm, $h = 8.88$ mm. Young's Modulus E is 200 GPa, and Poisson's ratio ν is 0.3.

The curve shown in Figure 8 can be obtained by theoretical settlement of the model parameters.

It can be seen from the figure that when the ribbon spring is affected by the reverse bending moment, the required driving bending moment increases sharply to a certain value $M_+^{\max}$ in the initial stage, which is called the critical bending moment. After this stage, the stiffness decreases rapidly, and the bending moment finally stabilizes to a certain value M_+^*, which is called the steady-state bending moment.

According to the theory, the bending-curvature diagrams of the three structures are shown in Figure 8. The critical bending moment values of the three structures ($M_+^{\max}$) are 6664.5 Nmm, 568.6 Nmm, 2068.2 Nmm, respectively. The steady-state bending moments are 956.5 Nmm, 121.3 Nmm, and 229.3 Nmm, respectively. Compared with the traditional structure, the support stiffness of the B-type honeycomb is higher than that of the A-type honeycomb. The three structural change processes are approximated to a locked state before reaching the critical bending, and buckling deformation occurs after reaching the critical bending; the stiffness decreases rapidly and finally reaches its steady-state bending moment value, which is beneficial to the dynamic characteristics required in the space deployment mechanism.

3. Numerical Argument Analysis

After determining the material properties and size parameters of the ribbon spring, a finite element model was established using ABAQUS software and the reverse bending process was simulated.

The whole model adopts the shell element S4R5, which is a 4-node reduced integral element with 5 degrees of freedom at each node on the element, which is suitable for analyzing small strain and large deformation problems. The finite element model is shown in Figure 9.

In order to facilitate the application of loads and constraints, the centroid nodes on both ends of the ribbon spring are connected by MPC constraints, respectively. The RBE2 rigid element is selected as the MPC type, and the shell restricts the 6 degrees of freedom of the nodes. Apply the displacement constraint 1.57 rad in the centroid of the section in the x-axis. The model dimensions are shown in Table 1.

The finite element models of A-type and B-type honeycomb belt springs were established with reference to the ordinary belt spring steel finite element model as shown in Figure 10.

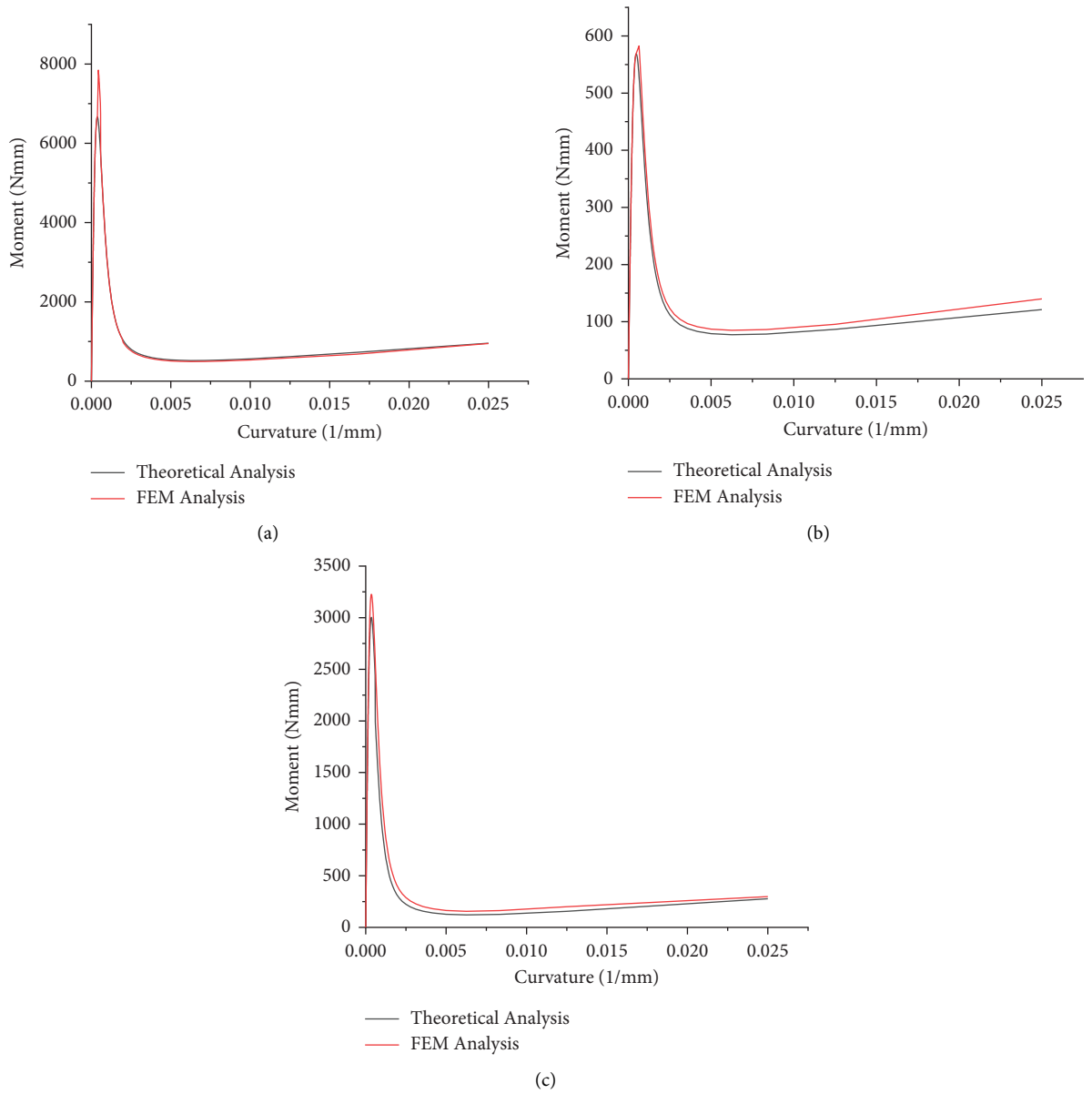

Figure 13: The comparison of theoretical analysis and FEM analysis of different structures. (a) Tape spring. (b) Model a. (c) Model b.

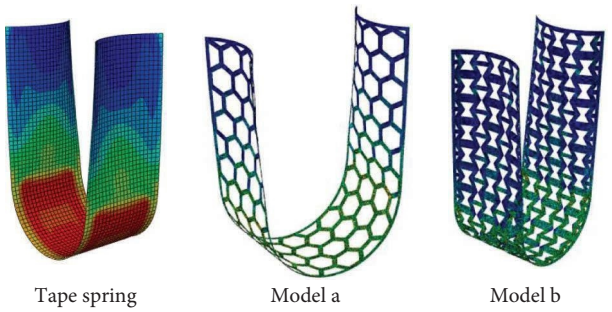

Figure 14: The optimization FEM for different structures.

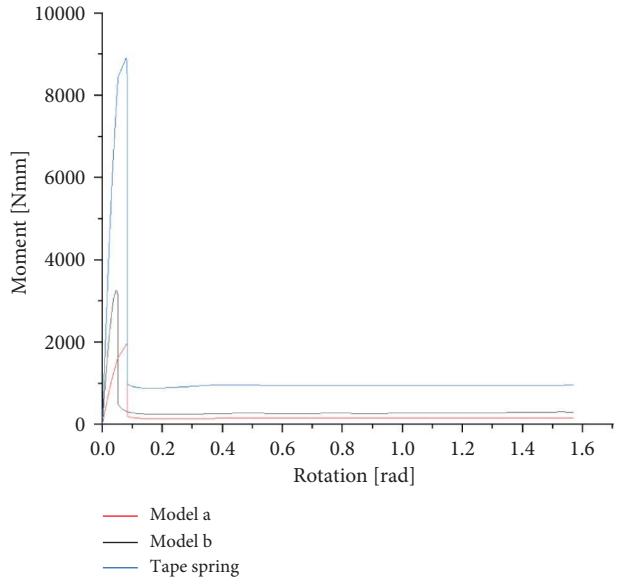

Figure 15: The moment-rotation angle relationships for different structures.

Table 2: Comparison of mass, critical bending moment, and steady-state bending moment of different structures.

	Mass (g)	Maximum moment (Nmm)	Steady moment (Nmm)
Tape spring	53.625	8909.3	950.3
Model a	7.537	1952.6	140
Model b	12.086	3264.2	305.7

It can be seen from Figure 11 that in the reverse bending process, before loading, the stress everywhere is 0, and the shell is not deformed. During the loading process, the stress in the middle of the shell gradually increases and expands to the width of the shell. As the rotation angle gradually increases, the stress value also increases. Finally, the model is stable, and the stress concentration area resembles a rectangle.

The reverse bending process is analyzed, and the corner bending moment curve is obtained as shown in Figure 12. From Figure 13, the moment variations of different model have the similar trend for FEM simulations and theoretical prediction. Overall, it is a good match between the two results.

Considering its application in engineering, we have added the frame in the honeycomb structures to improve its stability as shown in Figure 14.

It can be seen from Figure 15 that the common spring steel band spring reaches the maximum critical bending moment of 8909.3Nmm at a turning angle of 0.079 radian, and the steady-state bending moment is 950.3 Nmm; Model a reaches the maximum critical bending moment of 1952.6 Nmm at a turning angle of 0.081 radian, and the error steady-state bending moment is 305.7 Nmm; Model b reaches the maximum critical bending moment of 3264.2 Nmm at a turning angle of 0.045 radian, and the steady-state bending moment is 305.7 Nmm. The critical bending moment of the finite element is larger than the theoretical calculation because (19) assumes an infinitely long open cylindrical shell, thus ignoring the effect of the boundary conditions imposed on the end of the cylindrical shell, whereas the finite element model assumes a cylindrical shell of finite length and requires the use of some rigid constraints at the ends to apply moments. The bending trends of the three structures are consistent throughout the reverse buckling process.

Table 3: Comparison of critical bending moment and steady-state bending moment under unit mass of different structures.

	Maximum moment/mass	Steady moment/mass
Tape spring	166.1408	17.72121
Model a	259.0686	18.57503
Model b	270.0811	25.29373

From Table 2, it can be obtained that Model a reaches 21.9% of the critical bending moment and 14.7% of the steady-state bending moment performance of the ordinary spring steel cylindrical shell with 12.8% of the mass. Model b has better mechanical properties than Model a, reaching 36.6% of the critical bending moment performance and 32.2% of the steady-state bending moment performance of the ordinary spring steel cylindrical shell with 22.5% of the mass. An index unit mass "bending moment/mass" is proposed to measure this, and the mechanical properties of the honeycomb structure per unit mass are more excellent and have a better substitution effect. Table 3 shows the mechanical properties of different models per unit mass.

4. Conclusion

In this paper, according to the orthotropic shell bending theory, the calculation formula of the bending moment of the ribbon spring with honeycomb topology under orthotropic material is deduced. The sensitive parameters affecting the mechanical properties of the honeycomb topology ribbon spring can be obtained by the formula, and its bending moment variation trend and critical bending moment value during the reverse buckling process can be estimated; then, finite element analysis was carried out.

The final results show that the honeycomb structure has better mechanical properties per unit mass by proposing the unit mass index for analysis and comparison. Compared with the ordinary honeycomb structure of Model a, the negative Poisson's ratio honeycomb structure of Model b can achieve certain mechanical properties of the original ribbon spring with a lighter mass. Through the correctness and consistency of theoretical analysis and finite element modeling, the honeycomb topology has a good substitute value in the ribbon spring of the space deployment mechanism.

Data Availability

The data that support the findings of this study are available from the corresponding author upon reasonable request.

Conflicts of Interest

The authors declare that they have no conflicts of interest.

References

[1] R. Wu, P. C. Roberts, C. Soutis, and C. Diver, "Flexible heat shields deployed by centrifugal force," *Acta Astronautica*, vol. 152, pp. 78–87, 2018.

[2] J. Xiong and R. Shenoi, "General aspects on structural integrity," *Chinese Journal of Aeronautics*, vol. 32, no. 1, pp. 114–132, 2019.

[3] H. Huang, F. L. Guan, L. L. Pan, and Y. Xu, "Design and deploying study of a new petal-type deployable solid surface antenna," *Acta Astronautica*, vol. 148, pp. 99–110, 2018.

[4] J. Cai, Z. Ren, Y. Ding, X. Deng, Y. Xu, and J. Feng, "Deployment simulation of foldable origami membrane structures," *Aerospace Science and Technology*, vol. 67, pp. 343–353, 2017.

[5] Z. Chu, Z. Deng, X. Qi, and B. Li, "Modeling and analysis of a large deployable antenna structure," *Acta Astronautica*, vol. 95, pp. 51–60, 2014.

[6] L. Puig, A. Barton, and N. Rando, "A review on large deployable structures for astrophysics missions," *Acta Astronautica*, vol. 67, no. 1-2, pp. 12–26, 2010.

[7] M. Leipold, H. Fichtner, B. Heber et al., "Heliopause explorer—a sailcraft mission to the outer boundaries of the solar system," *Acta Astronautica*, vol. 59, no. 8-11, pp. 785–796, 2006.

[8] J. Block, M. Straubel, and M. Wiedemann, "Ultralight deployable booms for solar sails and other large gossamer structures in space," *Acta Astronautica*, vol. 68, no. 7-8, pp. 984–992, 2011.

[9] S. Ramayanti and P. Budiantoro, "Design analysis of solar panel structure LAPAN-Constellation Satellite using finite element method," in *Proceedings of the IOP Conference Series: Materials Science and Engineering*, IOP Publishing, Bristol, UK, February 2021.

[10] W. Gu, J. Zhang, L. Pan, Y. Qu, J. H. Choi, and X. Zhu, "Coupling effect of nonlinear stiffness of tape spring hinges and flexible deformation of panels during orbit maneuvers," *Aerospace*, vol. 9, no. 1, p. 30, 2022.

[11] K. Seffen, Z. You, and S. Pellegrino, "Folding and deployment of curved tape springs," *International Journal of Mechanical Sciences*, vol. 42, no. 10, pp. 2055–2073, 2000.

[12] S. J. Walker and G. S. Aglietti, "An investigation of tape spring fold curvature," in *Proceedings of the Int Conf Dyn Control Syst Struct Space*, Citeseer, Princeton, NJ, USA, March 2004.

[13] O Soykasap, "Analysis of tape spring hinges," *International Journal of Mechanical Sciences*, vol. 49, no. 7, pp. 853–860, 2007.

[14] O Soykasap, "Folding design of composite structures," *Composite Structures*, vol. 79, no. 2, pp. 280–287, 2007.

[15] G. F. Xuan Jican and J. Wang, "Yielding control of tape spring for deployable structures during the pure bending buckling," *Spatial Structures*, vol. 15, no. 4, 2009.

[16] F. Dewalque, J. P. Collette, and O. Brüls, "Mechanical behaviour of tape springs used in the deployment of reflectors around a solar panel," *Acta Astronautica*, vol. 123, pp. 271–282, 2016.

[17] F. Dewalque, P. Rochus, and O. Brüls, "Importance of structural damping in the dynamic analysis of compliant deployable structures," *Acta Astronautica*, vol. 111, pp. 323–333, 2015.

[18] F. Dewalque, C. Schwartz, V. Denoël, J. L. Croisier, B. Forthomme, and O. Bruls, "Experimental and numerical investigation of the nonlinear dynamics of compliant mechanisms for deployable structures," *Mechanical Systems and Signal Processing*, vol. 101, pp. 1–25, 2018.

[19] Y. D. Zuo, Z. X. Li, X. G. Xie, G. Jin, and P. Xie, "Characteristic calculation and experiment of CFRP lenticular tape spring," *Optics and Precision Engineering*, vol. 25, no. 2, pp. 385–393, 2017.

[20] C. Ensarioglu, A. Bakirci, H. Koluk, and M. C. Cakir, "Metal foams and their applications in aerospace components," *Materials, Structures and Manufacturing for Aircraft*, pp. 27–63, Springer, Berlin, Germany, 2022.

[21] S. W. K. Roper, H. Lee, M. Huh, and I. Y. Kim, "Simultaneous isotropic and anisotropic multi-material topology optimization for conceptual-level design of aerospace components," *Structural and Multidisciplinary Optimization*, vol. 64, no. 1, pp. 441–456, 2021.

[22] I. Masters and K. Evans, "Models for the elastic deformation of honeycombs," *Composite Structures*, vol. 35, no. 4, pp. 403–422, 1996.

[23] D. Chen and S. Ozaki, "Analysis of in-plane elastic modulus for a hexagonal honeycomb core: effect of core height and proposed analytical method," *Composite Structures*, vol. 88, no. 1, pp. 17–25, 2009.

[24] L. J. Gibson, M. F. Ashby, G. Schajer, and C. I. Robertson, "The mechanics of two-dimensional cellular materials," *Proceedings of the Royal Society of London A Mathematical and Physical Sciences*, vol. 382, no. 1782, pp. 25–42, 1982.

[25] W. Warren and A. Kraynik, "Foam mechanics: the linear elastic response of two-dimensional spatially periodic cellular materials," *Mechanics of Materials*, vol. 6, no. 1, pp. 27–37, 1987.

[26] H. G. Allen, *Analysis and Design of Structural sandwich Panels: The Commonwealth and International Library: Structures and Solid Body Mechanics Division*, Elsevier, Netherlands, 2013.

[27] W. Burton and A. Noor, "Assessment of continuum models for sandwich panel honeycomb cores," *Computer Methods in Applied Mechanics and Engineering*, vol. 145, no. 3-4, pp. 341–360, 1997.

[28] Y. Tanimoto, T. Nishiwaki, T. Shiomi, and Z. Maekawa, "A numerical modeling for eigenvibration analysis of honeycomb sandwich panels," *Composite Interfaces*, vol. 8, no. 6, pp. 393–402, 2001.

[29] L. Guj and A. Sestieri, "Dynamic modeling of honeycomb sandwich panel," *Archive of Applied Mechanics*, vol. 77, no. 11, pp. 779–793, 2007.

[30] F. Minghui, "Equivalent elastic parameters of the honeycomb core," *Acta Mechanica Sinica*, vol. 1, pp. 113–118, 1999.

[31] L. Mingjin, *Study of mechanics characteristics of negative Poisson's ratio honeycomb core structure*, University of Science and Technology of China, Hefei, China, 2012.